Spiral FFAG lattice design tools - Application to 6-D tracking

J. Fourrier, F. Martinache, F. Méot, J. Pasternak

Note LPSC 07-40 (RACCAM)

Spiral FFAG lattice design tools
Application to 6-D tracking

J. Fourrier[†], F. Martinache[†] F. Méot[‡], J. Pasternak[†]

[†] *CNRS IN2P3, LPSC, Grenoble*
[‡] *CEA et IN2P3, LPSC, Grenoble*

Abstract

Ray-tracing based methods for 3-D modeling of magnetic field and particle motion in spiral scaling FFAG accelerators have been developed. They allow efficient simulation of particle motion in presence of the strong field non-linearities proper to FFAG magnets, and of possible field overlapping in configurations of neighboring magnets, thus yielding a performing tool for spiral FFAG lattice design and optimizations, and for 6-D tracking studies. It is applied for illustration to a principle design of a 200 MeV medical class proton FFAG now under study in the frame of the RACCAM hadrontherapy project.

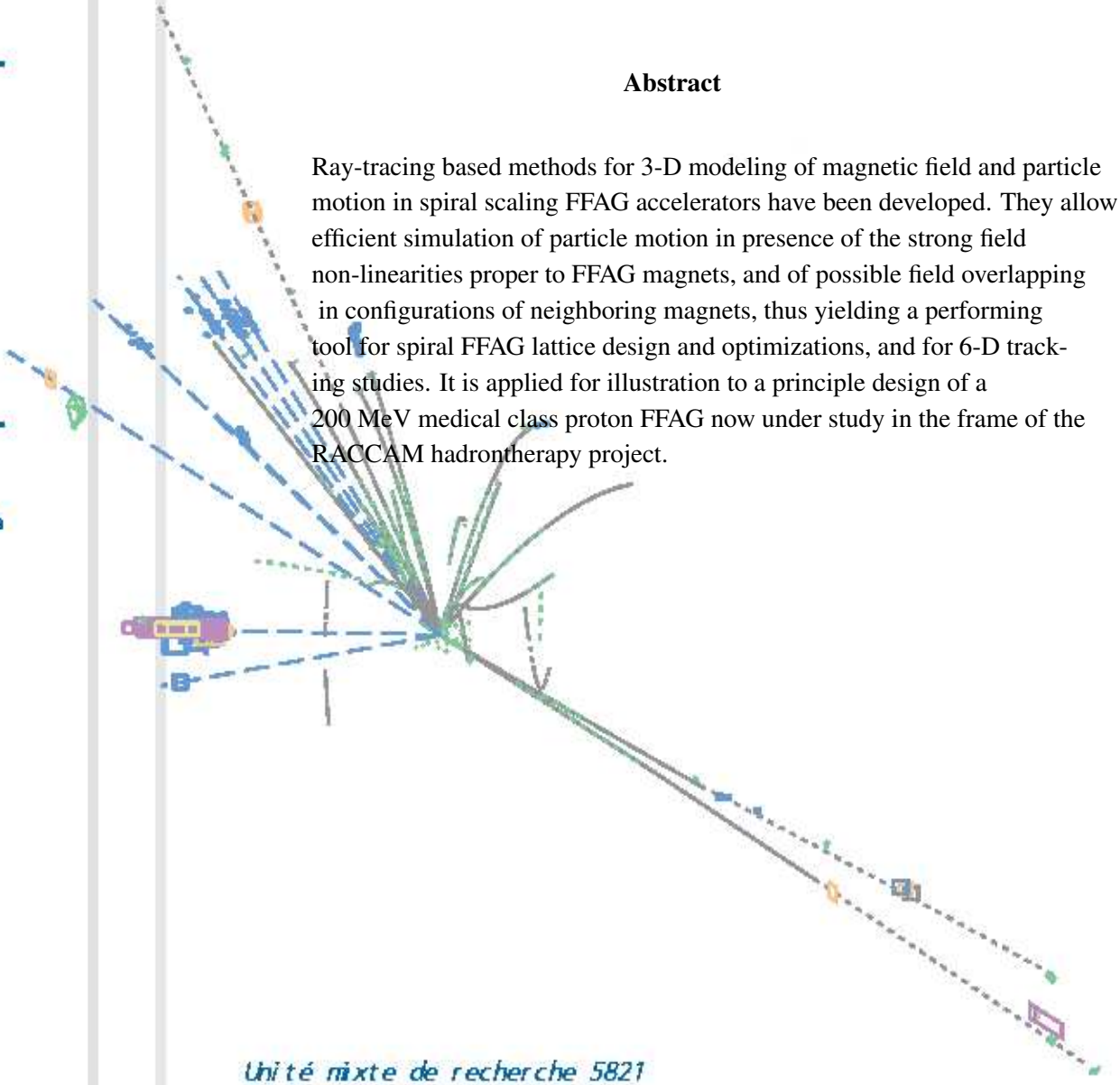

Laboratoire de Physique Subatomique et de Cosmologie

Unité mixte de recherche 5821

CNRS-IN2P3 / UJF / INPG

Contents

1 Introduction

Fixed field alternating gradient accelerators are nowadays subject to intense activities [1] in various domains as the acceleration of unstable beams [2, 3, 4], high power beams [5], neutron production [6], BNCT [7] as well as hadrontherapy uses [8].

In the context of these collaborations, and in particular that of the RACCAM FFAG project [9, 10], works have recently been undertaken concerning ray-tracing code developments regarding spiral FFAG lattice, in view of medical machine design in the short term, and possible application to muon rings for the scaling FFAG based neutrino factory, as well as high-power beams, in the longer term.

A good knowledge of FFAG accelerator parameters can only be drawn from stepwise ray-tracing in realistic field models. In particular this is the only method that allows computation of the dynamical acceptance of the ring. The developments presented here concern the implementation of such FFAG dedicated tools in the computer code Zgoubi [11, 12]. This has various outcomes, as offering means for fast optimization of magnet geometry and fields as constrained by accelerator design parameters ; providing correct computation of periodic motion, tunes, amplitude and momentum detunings, time of flight, etc. ; yielding precision tool for 6-D multiturn tracking, resonance and dynamic aperture studies. In addition, preliminary adjustments of magnet/field parameters can be performed thanks to the built-in fitting procedure, whereas optimizations based on 3-D magnet code calculations have the inconvenience of being slow and lacking flexibility in that matter.

The paper is organized as follows. Section 2 describes the main ingredients and methods in the modeling of spiral FFAG magnets. Section 3 shows an application to design issues, from determination of first order parameters to dynamic aperture scan. Section 4 discusses longitudinal dynamics and 6-D simulations.

2 A spiral magnet procedure

This Section describes the way the vertical field component $B_z(r,\theta)$ and derivatives at all position in the median plane of a magnet composed of neighboring spiral sectors (Fig. 1) with possibly overlapping fields are calculated, thus allowing the calculation of the field vector and its derivatives, as involved in the ray-tracing numerical method [11].

The various magnetic sectors are positioned within an angular domain AT, in the cylindrical frame with origin O at the center of the ring, using a reference radius R_0 and positioning angles ACN_i (Fig. 1).

The $B_z(r,\theta)$ calculation method is derived from an existing procedure regarding radial type FFAG magnets, presented in an earlier works [12], and yields a new routine, referred to as "`FFAG-SPI`" in the following.

The main ingredients are as follows. The magnetic field in the median plane ($z = 0$) of a spiral sector, in cylindrical coordinates (r,θ) (Fig. 2), is written

$$B_z(r,\theta) = B_{z0}\,\mathcal{F}(r,\theta)\,\mathcal{R}(r) \tag{1}$$

wherein B_{z0} is a reference field taken at reference radius R_0. The factor $\mathcal{R}(r)$ models the r dependence of the field, and can be expressed under either form

$$\mathcal{R}(r) = \left(\frac{r}{R_0}\right)^{k(r)} \quad \text{or} \quad \mathcal{R}(r) = b_0 + b_1\frac{r-R_0}{R_0} + b_2\left(\frac{r-R_0}{R_0}\right)^2 + ... \tag{2}$$

with $k(r)$ being the field index. Note that in the classical scaling FFAG optics k is in principle a constant, however in the present numerical approach it is allowed to be dependent of r : this permits designing possible compensation of the alteration of scaling properties under the effects of fringe field shape and extent, see below.

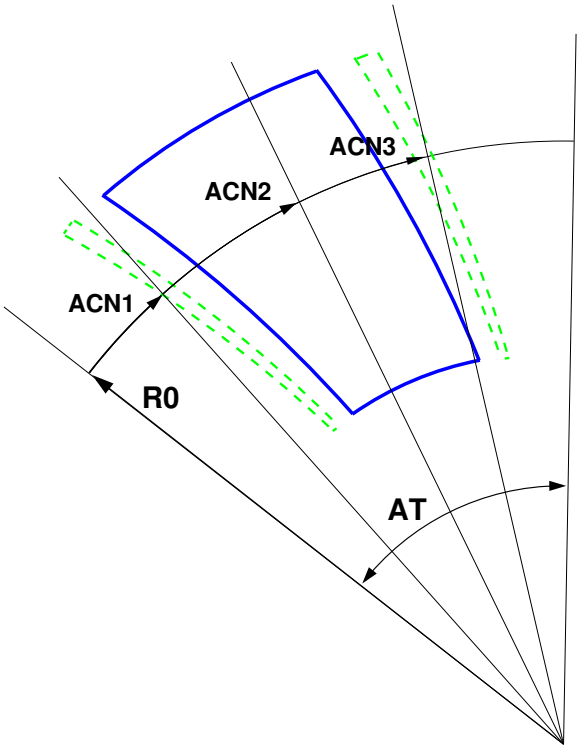

Figure 1: Definition of a spiral FFAG magnet, using the "`FFAG-SPI`" procedure. Several sectors with overlapping fields (clamps, here) can be accounted for.

The magnet *EFBs* have a spiral geometry with equation $r = R_0 e^{b(r)\theta}$, with $b(r) = 1/\tan\xi(r)$ and $\xi(r)$ the spiral angle. In principle again ξ is constant, however `FFAG-SPI` allows r-dependence, so to provide a mean for recovering scaling properties in case of perturbating effects as fringe fields, r-dependence of k, etc. The ensuing axial field form factor $\mathcal{F}(r,\theta)$ (sometimes modelled in analytical approaches by $1 + f\ \sin(N(\theta - \tan\xi \ln(r/r_0)))$, for a N sectors ring, with f the "flutter" [13]), gives the spiral azimuthal dependence of the field, and in the present ray-tracing tools is modelled in the way detailed below.

Field fall-offs The field fall-off (Fig. 3) at a particular effective field boundary (*EFB*) is written [14, p. 240]

$$\mathcal{F}_{EFB}(d) = \frac{1}{1+\exp[p(d)]}\ , \quad p(d) = C_0 + C_1 d/g + \ \ldots\ + C_5 (d/g)^5 \tag{3}$$

wherein d is the distance to that *EFB* and depends on r and θ ($d_{En.}$ and $d_{Ex.}$ for respectively the entrance and exit *EFBs* in Fig. 2), and the coefficient g is normally homogeneous to the gap and can be a function of r, see below. The distance d is computed by numerically solving for θ the equation [15]

$$\begin{aligned}&(X_m - e^{b\theta}\, R_0 \cos(\omega+\theta))\,(b\, e^{b\theta}\, R_0 \cos(\omega+\theta) - e^{b\theta}\, R_0 \sin(\omega+\theta)) + \\ &(Y_m - e^{b\theta}\, R_0 \sin(\omega+\theta))\,(e^{b\theta}\, R_0 \cos(\omega+\theta) + b\, e^{b\theta}\, R_0 \sin(\omega+\theta)) = 0\end{aligned} \tag{4}$$

which tells that the normal to the spiral *EFB* at location θ contains the observation point, i.e. $m = (X_m, Y_m)$ (therein the angle ω is the *EFB* angular position in the reference frame). The numerical coefficients $C_0 - C_5$ are supposed to be known, for instance from prior matching with realistic fringe field data.

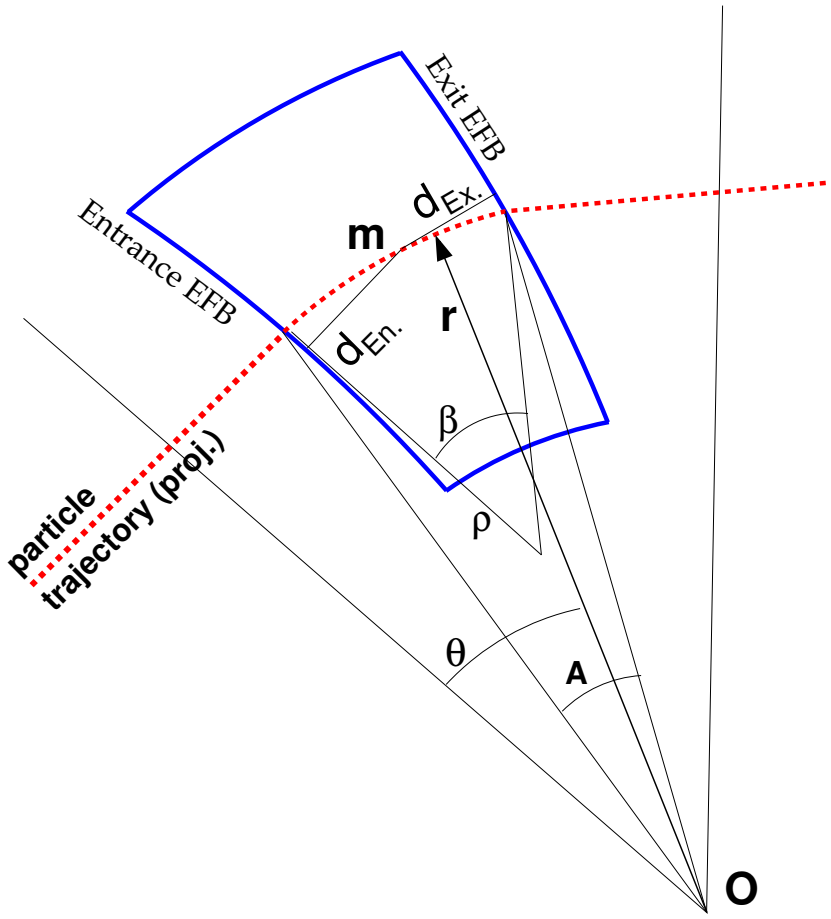

Figure 2: Ingredients entering in the computation of the mid-plane field $B_z(r,\theta)$ in a spiral sector magnet.

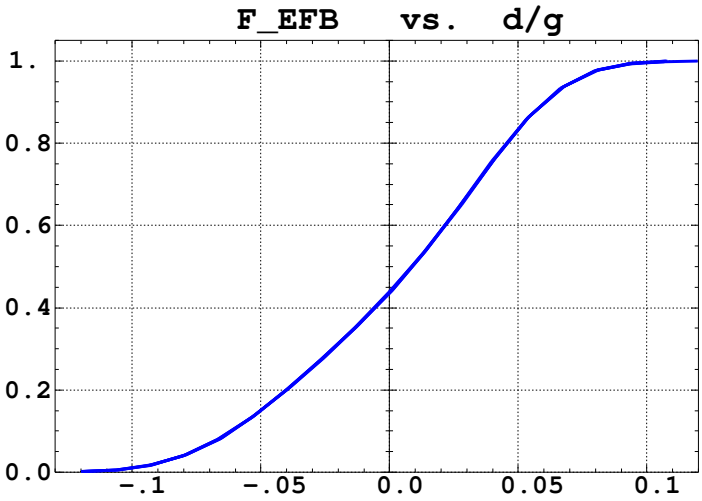

Figure 3: Typical fringe field shape, $\mathcal{F}_{EFB}(d/g)$ (Eq. 3).

Noteworthy, an adequate positioning of the *EFB* makes possible to satisfy (referring to the frame as defined in Fig. 3)

$$\int_{d=-\infty}^{0} \mathcal{F}_{EFB}(u)\, du = \int_{d=0}^{\infty} (1 - \mathcal{F}_{EFB}(u))\, du$$

which entails that varying g (as ensuing from r dependence, for instance, see Eq. 5) will not change the magnetic length, it will only change the fall-off steepness. This has the convenient consequence of allowing the simulation of various gap geometries as

$$\begin{array}{lll} g(r) = g_0(R_0/r)^\kappa, \quad \kappa \approx k & & \text{gap shaping} \\ g(r) = C^{st} & (\kappa = 0) & \text{parallel gap} \\ g(r) = g_0\, r/R_0 & (\kappa = -1) & \text{linear gap} \end{array} \tag{5}$$

From a practical point of view, the first $g(r)$ dependence simulates the case where the field law $B_z(r) = B_{z0}(r/R_0)^k$ ensues from the gap shape (so called "gap-shaping" method), whereas in the second and third cases $B_z(r)$ is supposed to be obtained from coil distributions in the gap. Note that the linear gap case ensures r-invariant vertical tune, as addressed in Section 3.

Both entrance and exit *EFBs* have their own fringe field factors, $\mathcal{F}_{\text{En.}}$, $\mathcal{F}_{\text{Ex.}}$. The form factor at particle position (r, θ) is thus written

$$\mathcal{F}(r, \theta) = \mathcal{F}_{\text{En.}}(r, \theta) \times \mathcal{F}_{\text{Ex.}}(r, \theta) \tag{6}$$

Full field at arbitrary position Now, accounting for n neighboring sectors (for instance, a main dipole and field clamps as schemed in Fig. 1), the mid-plane field and derivatives are computed by addition of the contributions of the $i = 1,\ n$ sectors taken separately, namely

$$B_z(r, \theta) = \sum_{i=1,n} B_{z\,0,i}\, \mathcal{F}_i(r, \theta)\, \mathcal{R}_i(r) \text{ and } \frac{\partial^{k+l} \vec{B}_z(r, \theta)}{\partial \theta^k \partial r^l} = \sum_{i=1,n} \frac{\partial^{k+l} \vec{B}_{z\,i}(r, \theta)}{\partial \theta^k \partial r^l} \tag{7}$$

Note that, in doing so it is not meant that linear field superposition actually applies, it is just meant to provide the possibility of obtaining a realistic field shape, that would for instance closely match (using adequate $C_0 - C_5$ sets of coefficients, Eq. 3) 3-D field distributions obtained from magnet codes or from measurements. This procedure is illustrated in

(i) Fig. 4 that shows the field distribution in the median plane of a spiral magnet with field index $k \approx 4$ and spiral angle $\xi \approx 50$ degrees,

(ii) Fig. 5 that shows the field resulting from the superposition of a central dipole and of field clamps (simulated as powered thin magnets) as schemed in Fig. 1.

The 6-D field $\vec{B}(r, \theta, z)$ **and derivatives** $\partial^{k+l+m} \vec{B} / \partial r^k \partial \theta^l \partial z^m$ at particle location are eventually deduced by z-extrapolation accounting for Maxwell equations [11, 12].

Calculation of the mid-plane derivatives (Eq. 7) can be performed using one or the other of the following methods, upon option,

(i) numerical interpolation from a "flying mesh". In this case $B_z(r, \theta, Z = 0)$ is computed at the $n * n$ nodes ($n = 3$ or 5 in practice) of a "flying" interpolation mesh centered on the actual $(r, \theta, z = 0)$ particle position projection (m in Fig. 2).

(ii) use of a 2-D mid-plane magnetic field map (Fig. 4) that encompasses the all magnet, computed beforehand using the procedure above.

In addition, a third method is under installation, fully based on analytical expressions of $B_z(r, \theta)$ and derivatives $\partial^{i+j} B_z(r, \theta) / \partial r^i \partial \theta^j$, as was done for the radial FFAG magnet [12].

The first method has the merit of allowing parameter optimization using the built-in fit procedure. The second one has the merit of faster tracking. Both feature excellent symplecticity - dependent upon

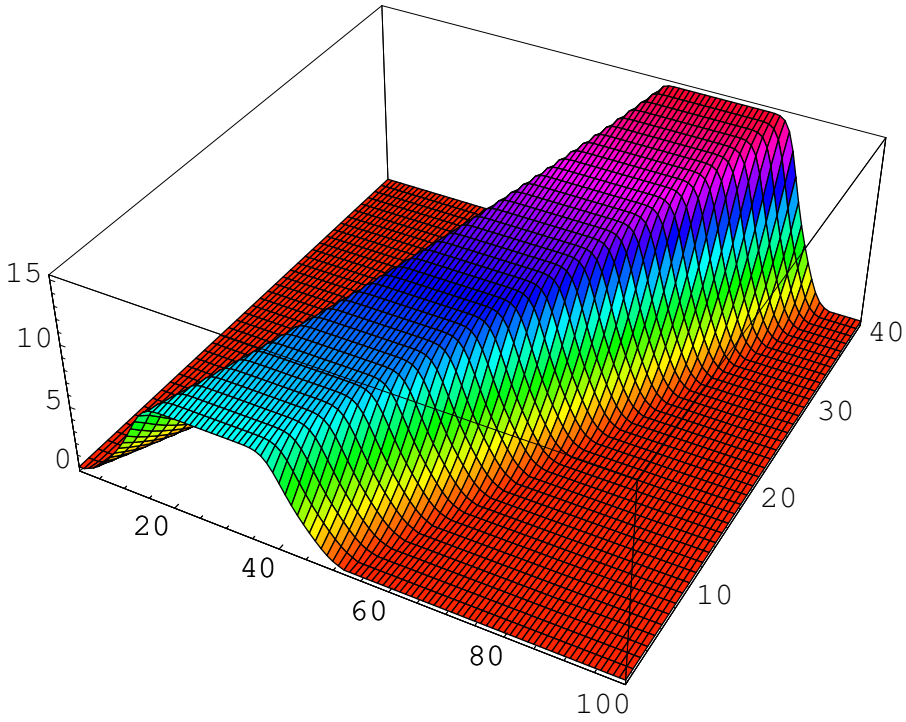

Figure 4: Spiral magnet field map as obtained from Eqs. 1-6.

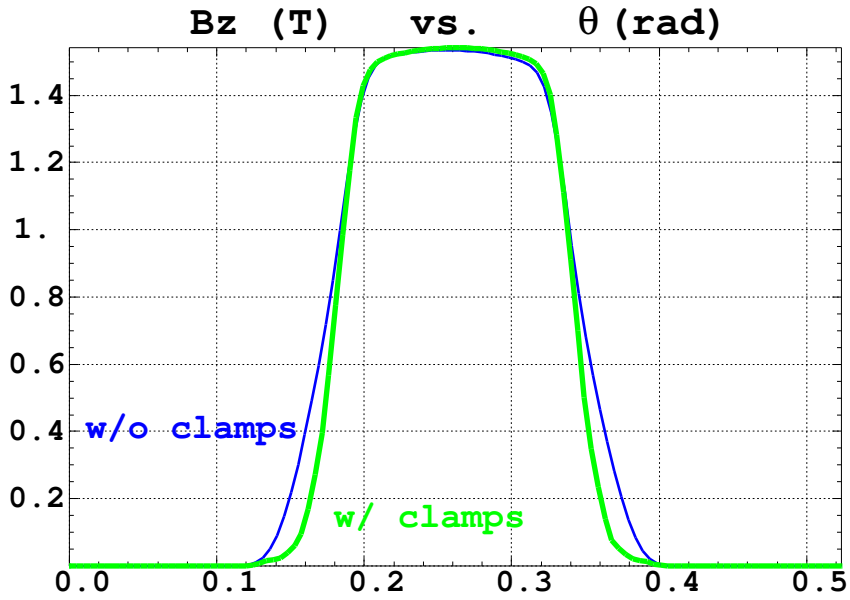

Figure 5: Typical axial dependence $B_z(r_0, \theta)$ (Eq. 7) of the mid-plane field, as observed at traversal of a spiral sector. The modeling of the effect of clamps is also shown.

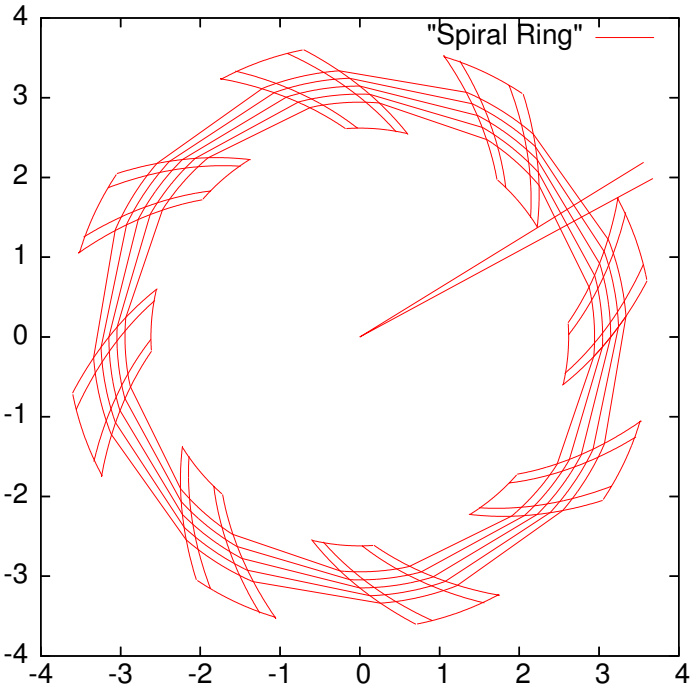

Figure 6: Spiral ring and a set of closed orbits taken between 0.6 T.m (17 MeV proton) and 2 T.m (180 MeV).

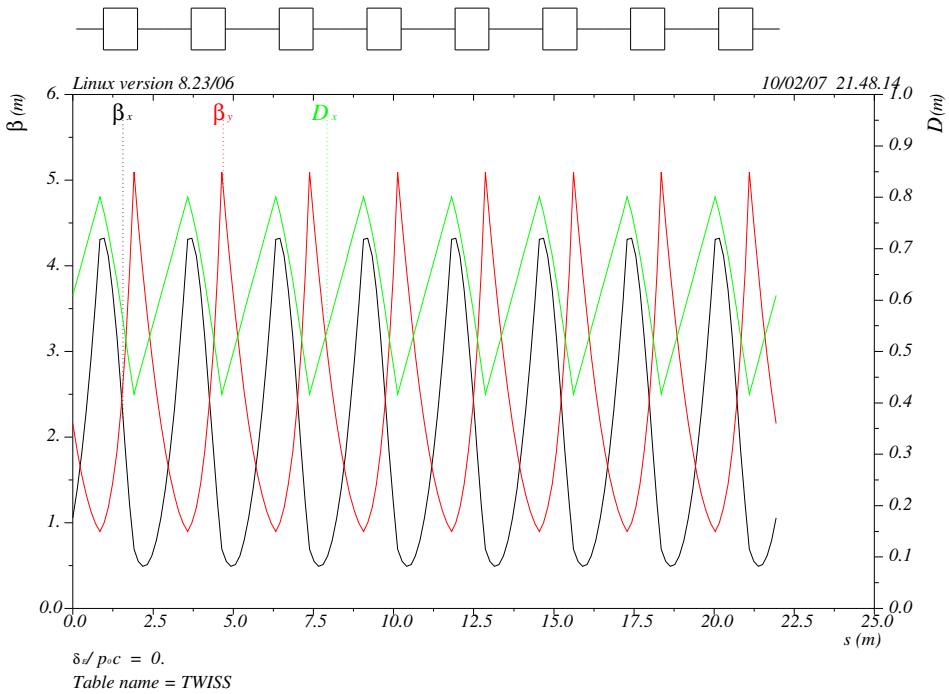

Figure 7: Typical optical functions in the smooth approximation, on innermost, 0.6 T.m orbit. Optical functions on outermost, 2 T.m orbit are similar with about 10% larger amplitude.

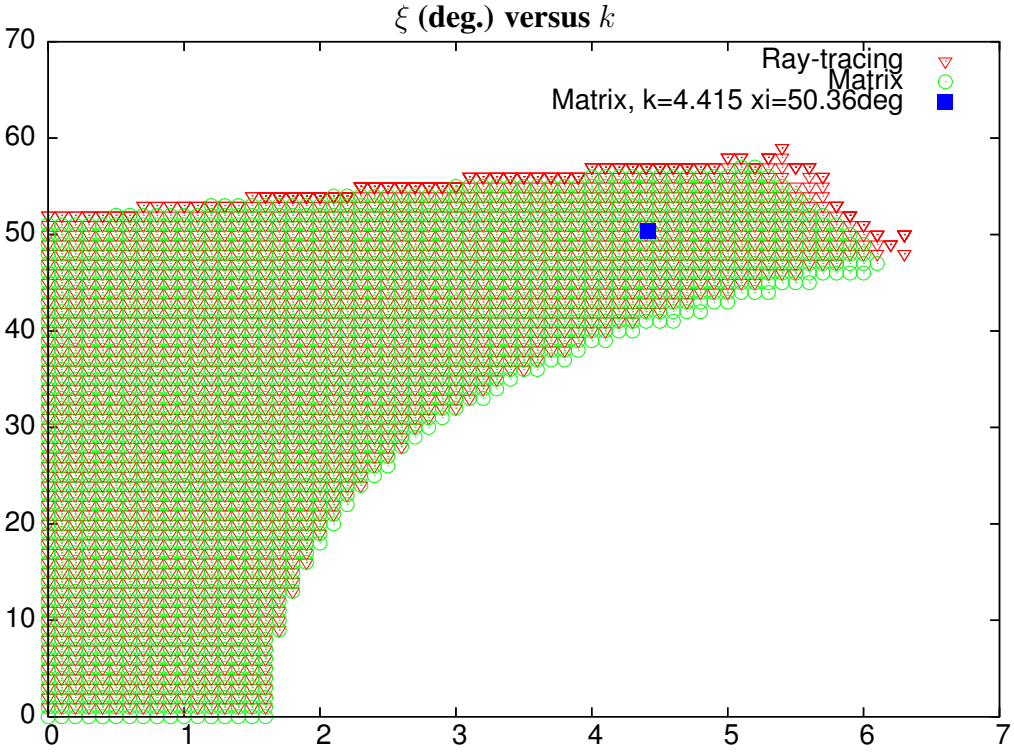

Figure 8: k, ξ stability domain. Circles : from matrix transport, triangles : from ray-tracing.

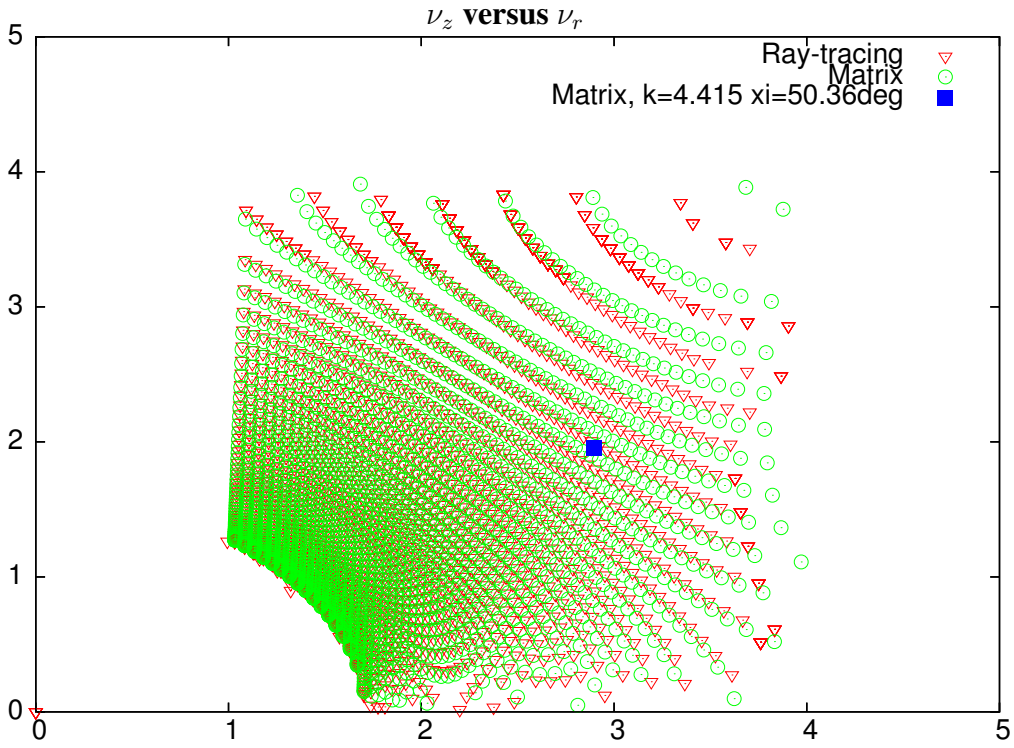

Figure 9: Tune diagram showing the periodic stability region. Circles : from matrix transport, triangles : from stepwise ray-tracing.

mesh size, integration step size. The third method has all the merits, speed, symplecticity, and its allowing automatic parameter fits.

3 Beam dynamics in a spiral ring

In this Section the numerical techniques described above are tested, with the goal of showing that this spiral magnet modelling allied with stepwise ray-tracing methods provide an efficient design tool. For that purpose a particular spiral FFAG geometry, representative of a protontherapy class machine, is submitted to various numerical experiments, as follows.

3.1 Magnet and ring geometry

The geometry and parameters of the N-sector lattice of concern are shown in Fig. 6. The magnets occupy a fraction ("packing factor") $pf = 0.38$ of the circumference, independent of radius, a scaling property. The extreme radii and rigidities satisfy, another scaling property, $B\rho_2 \ / \ B\rho_1 = (r_2/r_1)^{k+1}$. In the smooth approximation, the dipole sector angle A (Fig. 2) and bend angle $\beta = 2\pi/N$ are in the ratio pf ; the sector radius r and curvature radius ρ satisfy $r\sin(A/2) = \rho\sin(\beta/2)$.

Table 1: Parameters of the spiral ring.

number of cells N	8	
field index k	4.415	
spiral angle ξ	50.36	(deg.)
packing factor pf	0.38	
min.-max. radius $r_1 \ldots r_2$	$2.78 - 3.48$	(m)
min.-max. proton rigidity $B\rho_1,\ B\rho_2$	$0.6 - 2$	(T m)
corresponding kinetic energy	$17 - 180$	(MeV)
field at r_2	1.5	(T)
dipole sector angle A	17.1	(deg.)
dipole bend angle β	45.0	(deg.)

The smooth approximation allows deriving the optical functions on an arbitrary closed orbit (Fig. 7) with reasonable accuracy from matrix representation, with optical elements being the two end drifts $r\sin(\pi/N - A/2)$, dipole ends wedge angles $\epsilon_{Ex,En} = \pi/N - A/2 \pm \xi$, and the dipole body ρ, β.

A scan of the (k, ξ) space in the smooth approximation yields the stability region shown in Fig. 8 (circles), and the corresponding tune domain shown in Fig. 9. A similar (k, ξ) scan using the ray-tracing method and field modelling described in Section 2 has been superimposed (triangles in Figs. 8, 9). The agreement between both methods is good for lower k and ξ values and deteriorates with increasing k and with increasing ξ - this behavior will be devoted further investigation, however it could be attributed to (i) the loss of validity of the constant orbit radius assumption in the smooth approximation, *i.e.* closed orbits in the dipole sensibly depart from an arc of a circle, and to (ii) the increasing perturbative effect of fringe fields, as they are traversed over an increasingly long distance for larger ξ values.

It can be concluded at that stage that the consistency of the two types of results is good, so confirming the efficiency of the smooth approximation for a first approach of the magnet and lattice parameters, whereas the precision of ray-tracing is necessary for further insight into ring design and beam dynamics.

3.2 First order behavior

In the beam dynamics studies that follow we consider for illustration the particular optics $(k, \xi) = (4.415, 50.36\text{deg.})$, subject to extensive studies in the frame of the RACCAM project [9, 10] (the working point materialized by a square solid marker in Fig. 8). The corresponding tune values, using the `FFAG-SPI` method (respectively, in the matrix approximation) are $(\nu_r, \nu_z) = (2.817, 1.793)$ (respectively $(\nu_r, \nu_z) = (2.896, 1.952)$, square marker in Fig. 9). Fig. 7 displays the ensuing optical functions in the matrix approximation.

This optics accounts for fringe field extent at magnet ends as represented in Fig. 3, with gap proportional to radius ($g_0 = 3$ cm at $R_0 \equiv r_2 = 3.48$ m, $\kappa = -1$ in Eq. 5) thus yielding very weak sensitivity of vertical tune to radius[1] in addition to quasi-constant horizontal tune as ensuing from the property of zero chromaticity. Namely, the ray-tracing yields $(\nu_r, \nu_z) = (2.817, 1.793)$ at better than $\pm 3\,10^{-4}$ (relative) over the full radial extent $[r_1, r_2] = [2.78m, 3.48m]$.

Fig. 10 shows the radius value (taken to the center of the ring) along closed orbits over the $2\pi/8$ cell extent, at various momenta. It can be observed that the scaling rule $r/R_0 = (p/p_0)^{1/(k+1)}$ is satisfied with good precision ; indeed, inside the dipole (the θ regions with non-zero magnetic field, see Fig. 11), the closed orbit radius departs by no more than about $\pm 3\%$ from the theoretical, $r = C^{\underline{st}}$ smooth approximation value. Fig. 11 shows the magnetic field along those closed orbits.

The momentum compaction $\alpha = d\mathcal{L}/\mathcal{L} \,/\, dp/p$ can be numerically computed from Δp induced difference in closed orbit lengths. Sample values are given in Fig. 12, they are close to the theoretical value $\alpha \approx 1/(1+K)$.

All these results show good consistency and reasonable agreement between the smooth approximation data and numerical results, a property useful in preliminary design stages.

3.3 Large amplitude motion

The main goal in this section is to show the satisfactory behavior of the numerical spiral magnet modelling, and of the large amplitude multiturn tracking.

Fig. 13 shows horizontal phase space trajectories at the limit of stable motion in the ring, for various energies, as observed along a radial direction in the drift region ; the triangle shape of phase space motion is related to the presence of strong sextupole component in $B(r)$ (Eq. 2) and to the proximity to third integer cell tune ; the triangles rotate due to the change of focusing conditions along a radius (the focusing is invariant by a displacement $\Delta r, \Delta\theta = \tan(\xi)\ln((r+\Delta r)/r)$). Fig. 14 shows vertical phase space trajectories at the limit of stable motion in the ring, for three different energies, and with cell tune close to quarter integer.

Fig. 15 and Fig. 16 show horizontal and vertical phase space motion at 60 MeV, observed at the center of the drift ; the symplecticity is very good, up to stability limit. Another feature in these Figures is the large dynamical acceptance characteristic of FFAG optics : the surface of the 60 MeV stability limit portraits are $\epsilon_r \approx 1000\pi$ mm.mrad, $\epsilon_r \approx 200\pi$ mm.mrad. The corresponding amplitude detuning resulting from the non-linear field is shown in Fig. 17.

Fig. 18 shows the tune footprint of a monochromatic beam with size $\epsilon_r \approx \epsilon_z \approx 100\,\pi$ mm.rad, together with right and skew systematic resonance lines up to 6th order. Automatized tracking tools have been developed to scan the dynamic aperture in the vicinity of the working point in the tune diagram [16], typical results are shown in Fig. 19. This method is now routinely used in the design of the spiral magnet in the frame of the RACCAM project [9, 10].

[1] In the smooth approximation, this can be understood from the vertical wedge focusing, namely $(z'/z'_0) = \tan(\epsilon - \psi)/\rho)$, given the correction for the fringe field extent $\psi = I\frac{g}{\rho}\frac{1+\sin^2\epsilon}{\cos\epsilon}$, wherein I is a form factor, so that $g \backsim \rho = pf \times r$ yields r-independent ψ correction.

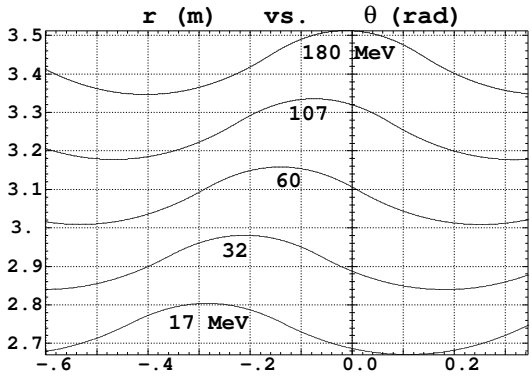

Figure 10: Radius value (taken to the center of the ring) along closed orbits, in a cell.

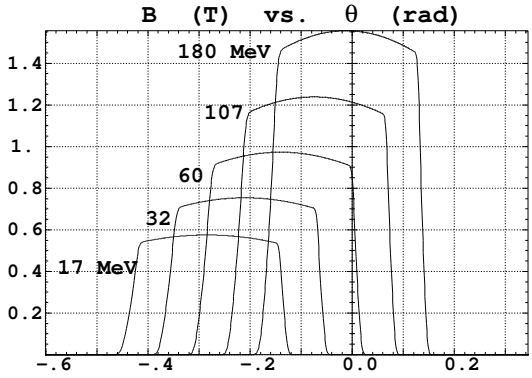

Figure 11: Magnetic field on closed orbits, along a cell.

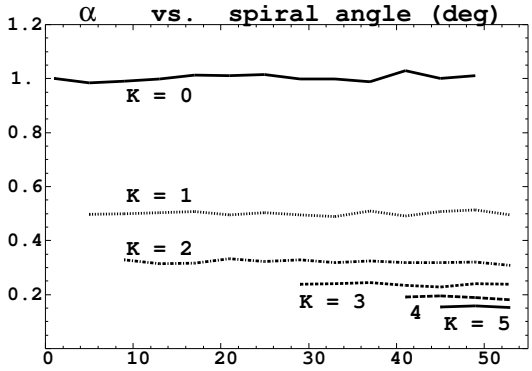

Figure 12: Momentum compaction behavior.

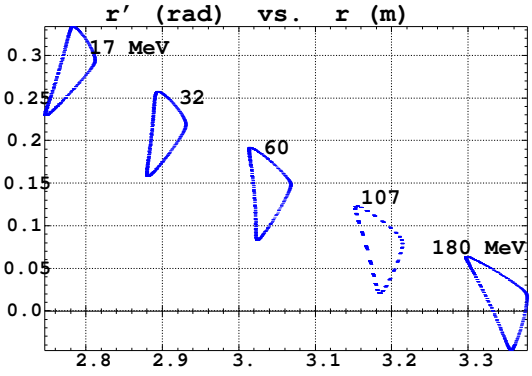

Figure 13: Horizontal stability limits, at 1 mm precision, 1000 cells, for various energies.

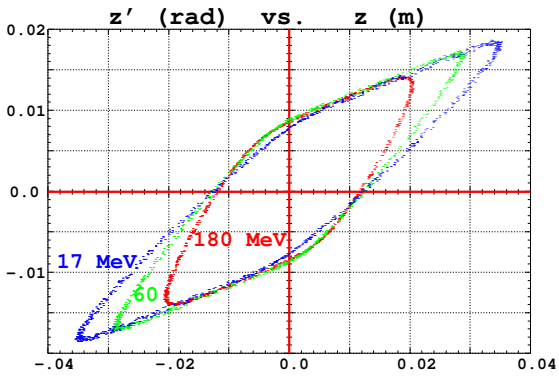

Figure 14: Vertical stability limits, at 1 mm precision, 1000 cells. Horizontal motion is near closed orbit.

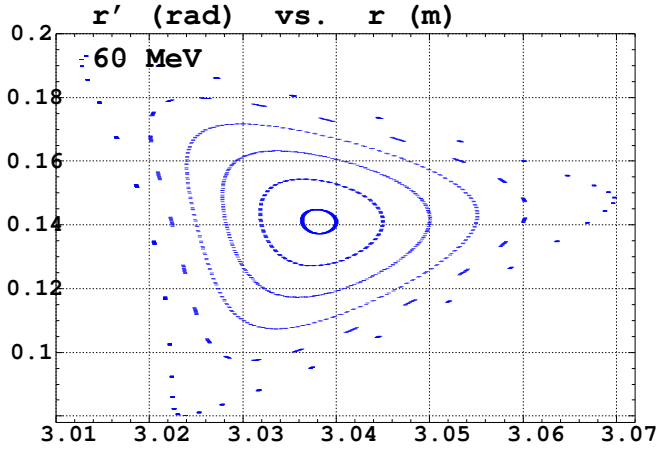

Figure 15: 60 MeV horizontal phase-space, up to $\approx 1000\,\pi$ mm.mrad maximum stable amplitude.

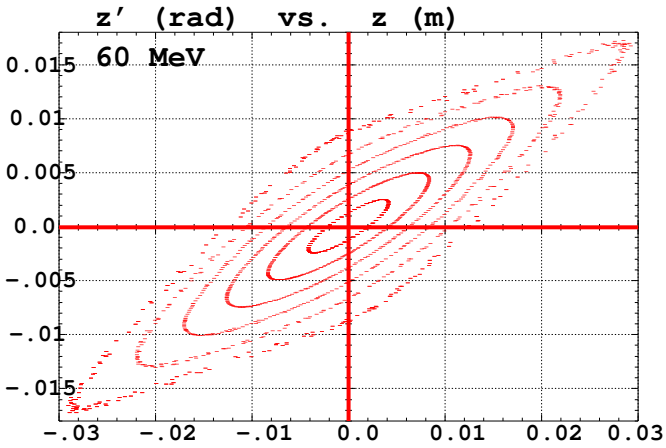

Figure 16: 60 MeV vertical phase-space, up to $\approx 200\,\pi$ mm.mrad maximum stable amplitude.

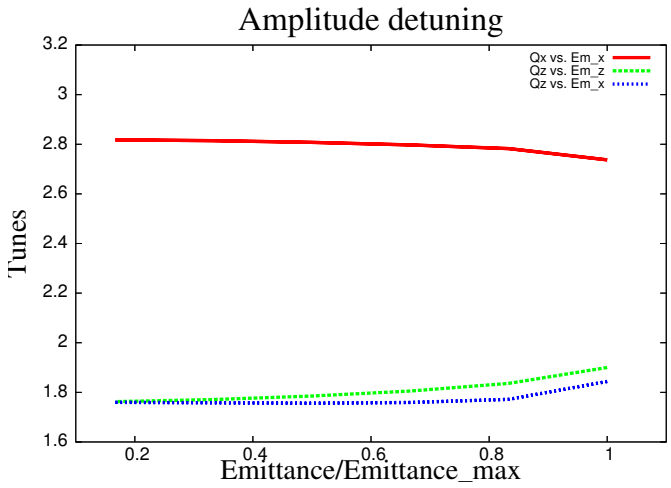

Figure 17: Amplitude detuning, from paraxial motion up to maximum stable amplitude. 60 MeV case.

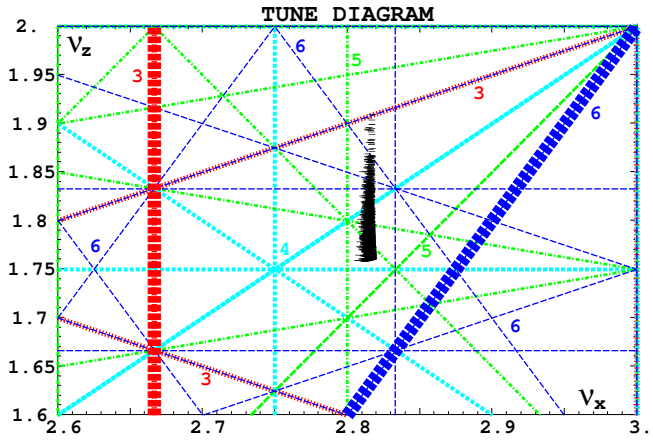

Figure 18: Beam occupation in tune diagram, due to amplitude detuning (given $\delta p/p \equiv 0$, $\epsilon_r \approx \epsilon_z \approx 100\,\pi$ mm.rad). Right + skew lines $m\nu_r + n\nu_z = p$ as well as $|m| + |n|$ values are shown ; the two thick lines are neighboring systematic resonances, $3\nu_r = 8$, $4\nu_r - 2\nu_z = 8$, .

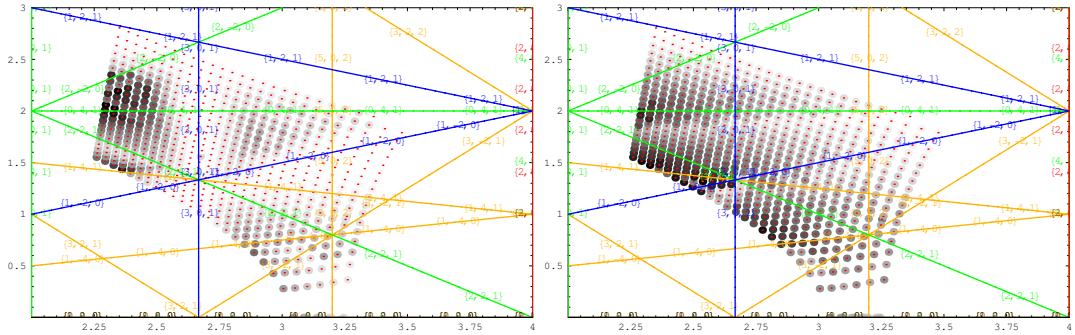

Figure 19: A scan of the dynamic aperture in the $(\nu_r, \nu_z) = (2.8, 1.8)$ region, (a) in case of horizontal motion with infinetisimal starting vertical emittance, (b) in case of pure vertical starting emittance.

4 Longitudinal motion

An RF gap is now introduced in the ring, as represented in Fig. 20.

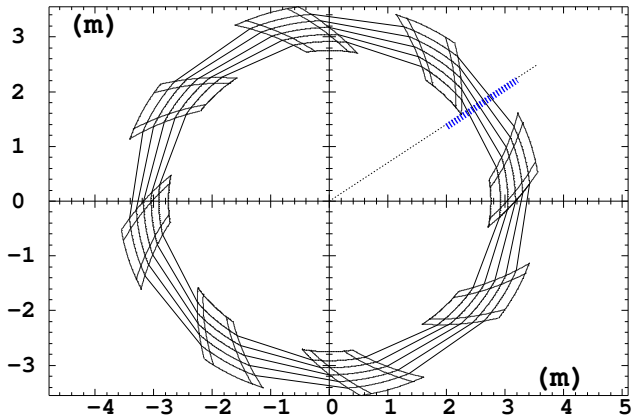

Figure 20: Positioning of the RF gap in a drift.

4.1 Stationary bucket

The RF gap is located in a drift, along a radius, orthogonal to the maximum energy closed orbit ($r \approx 3.4$ m, see Fig. 20). Injection orbit, 17 MeV, $\gamma = 1.01812$, $r \approx 2.75$ m, 17.33 m circumference, is considered. The peak RF voltage is $\hat{V} = 20$ kV, a value rather large for the sake of faster tracking. Other RF parameters are, $f_{RF} = 3.249$ MHz, harmonic=1, synchronous phase $\phi_s = 0$. These conditions yield theoretical momentum acceptance

$$\pm\frac{\Delta p}{p} = \pm\frac{1}{\beta_s}\left(\frac{2q\hat{V}}{\pi h\eta E_s}\right)^{1/2} \approx \pm 2.18\,\% \tag{8}$$

given $E_s = 955.27$ MeV synchronous energy, slippage factor $\eta = \frac{1}{\gamma^2} - \alpha = \frac{1}{\gamma^2} - \frac{1}{1+K} \approx 0.78$ with $K = 4.415$. The theoretical small amplitude synchrotron tune is

$$\nu_s = \frac{1}{\beta}\left(\frac{h\eta\cos\phi_s\, q\hat{V}}{2\pi E_s}\right)^{1/2} \approx 8.52\,10^{-3} \tag{9}$$

Both $\Delta p/p$ and ν_s values are in excellent agreement with values of bucket height and RF cycles per turn obtained from numerical simulations as shown in Fig. 21, namely $\pm\Delta p/p = \pm 2.20\%$ and $\nu_s = 1/117$ turns.

4.2 A full acceleration cycle

A particle is now launched with all starting coordinates zero except for $z_0 = 3$ mm.

From 17 to 180 MeV, the RF frequency is increased linearly with turn number from 3.25 to 7.51 MHz, at constant synchronous phase $\phi_s = 30$ degrees, $\hat{V} = 20$ kV, which means about 16000 turns to complete the cycle.

Fig. 22 shows the first synchrotron oscillation cycles, from 17 to 18.47 MeV, of $\pm 1\%$ off-momentum particles around a quasi-synchronous one. From the figure, the synchrotron period appears to be in agreement with Eq. 9, given the working hypothesis above.

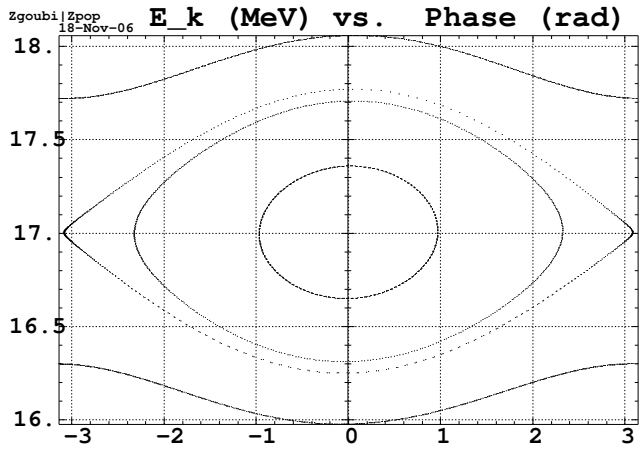

Figure 21: Stationary bucket on injection orbit.

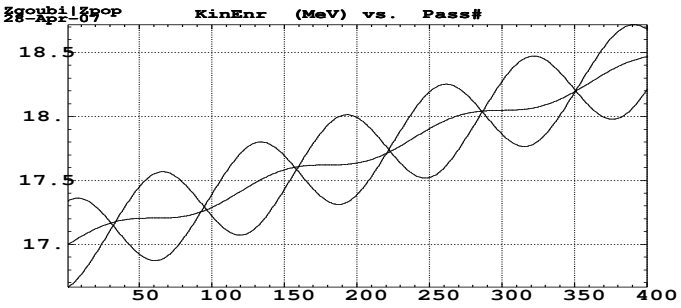

Figure 22: First 400 turns of an acceleration cycle in the 8-cell spiral ring. $dp/p \approx 10^{-3}$ and $\pm 1\%$.

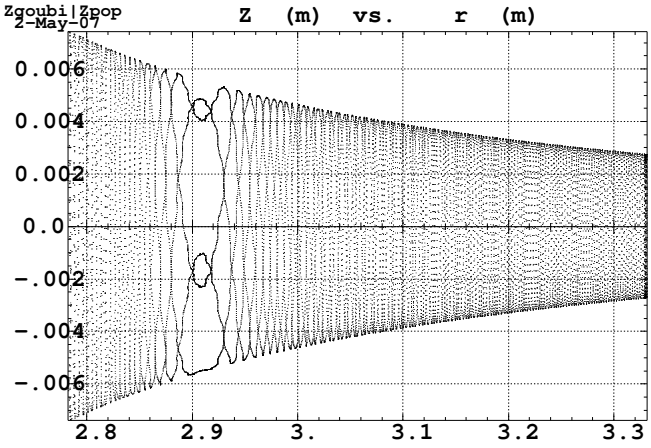

Figure 23: Adiabatic damping of vertical motion over an acceleration cycle.

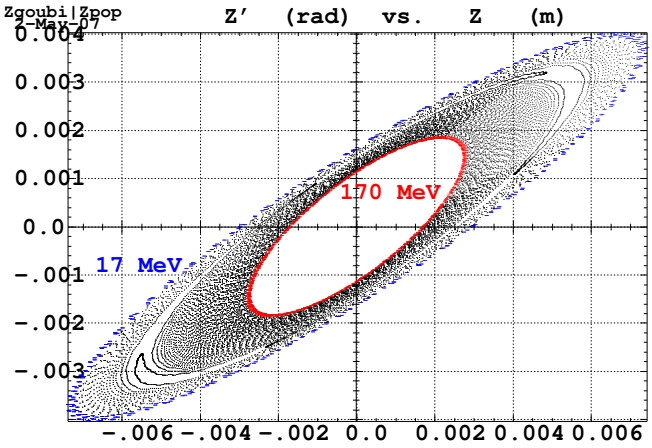

Figure 24: Adiabatic damping of vertical motion over an acceleration cycle (transverse phase space observed at fixed azimuth). Larger amplitude (resp. smaller) corresponds to injection (resp. final) energy.

Sample vertical motion is displayed in Figs. 23, 24 and shows excellent behavior. Regular damping can be observed, of the form $(B\rho_{170\,\mathrm{MeV}}/B\rho_{17\,\mathrm{MeV}})^{1/2} \approx \sqrt{3.3}$ from start to end of the cycle. Referring to Fig. 24, it yields a surface ratio of about 0.55 between the outer (17 MeV) ellipse and the inner one (170 MeV). Note that the ellipse rotates, since the observation is at fixed azimuth, as already pointed out concerning Figs. 13, 14.

4.3 Admittance at injection

Acceleration of 8000 particles over about 300 turns (from 17 MeV to about 18.1 MeV) is now performed. Acceleration conditions are the same as previously, Sec. 4.2. A 4-D mono-energetic bunch is considered, with transverse emittances far beyond dynamical aperture and non-correlated $x - z$ coordinates. In these conditions the bunch will be cleaned from all particles beyond 4-D dynamical aperure ; a few hundred turns is sufficient to ensure that cleaning, particle loss beyond that will not be significant, given that the optics does not strongly change in the course of acceleration as can be seen in Figs. 13, 14. The about 2003/8000 surviving particles give a reasonable image of the ring admittance at injection, which can be observed, in Figs. 25, 26, to be about

$$A_r \approx 900\,10^{-6}\pi \text{ m.rad, horizontal,} \quad A_z \approx 190\,10^{-6}\pi \text{ m.rad, vertical}$$

not so far from single energy estimates in Sec. 3.3 (Figs. 13-16).

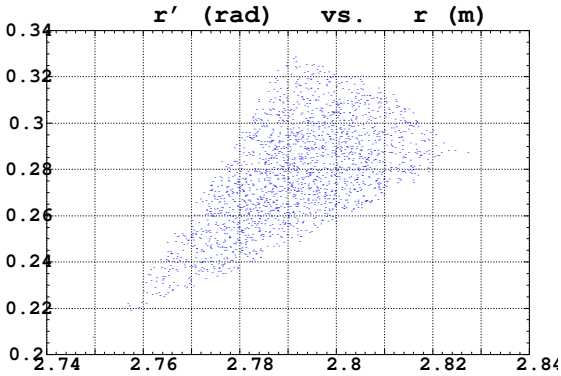

Figure 25: Horizontal admittance, 4-D case. Surface : $A_r/\pi \approx 900\,10^{-6}$m.rad.

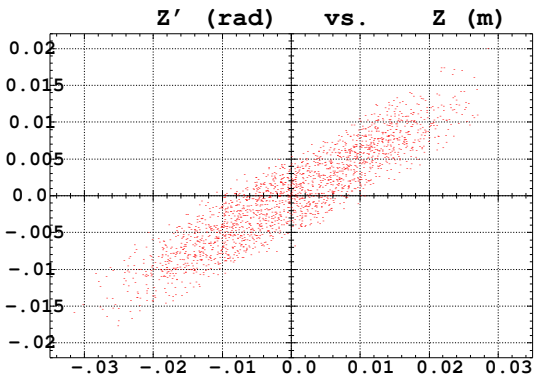

Figure 26: Vertical admittance, 4-D case. $A_z/\pi \approx 190\,10^{-6}$m.rad.

5 Conclusion

The developement of precision tracking tools presented here, a follow-on of an earlier work concerning radial FFAG lattice design [12], yields computing means now extensively used for spiral FFAG design [10]. In particular, they allow (i) providing benchmarking data in magnet design studies, and (ii) automatized matching of magnet and lattice parameters.

Not addressed here, automatized procedures for the injection of various type of defects (field, alignement, etc.) have been developped that allow statistical analysis and tolerance evaluations [17].

The code developped for this purpose, Zgoubi [11], also provides ray-tracing in 2-D and 3-D magnetic field maps, it can therefore as well be used as the ultimate design and beam dynamics studies tool prior to construction.

References

[1] The rebirth of the FFAG, M. Craddock, CERN Courrier 44-6 (2004) ;
see also, Fixed field alternating gradient synchrotrons, F. Méot, Invited talk, ICFA-HB2004 Workshop, Bensheim, 18-22 Oct. 2004.

[2] A feasibility study of a neutrino factory in Japan, KEK report, Feb. 2001.

[3] Feasibility Study-II of a Muon-Based Neutrino Source, ed., S. Ozaki et als., BNL-52623 (2001).

[4] Non-Scaling FFAGs for Radio-Isotopes Production, A.G. Ruggiero ; Non-scaling FFAG lattice design for the Radioactive Ion Accelerator, D. Trbojevic, FFAG 2007 Workshop, LPSC, Grenoble. http://lpsc.in2p3.fr/congres/FFAG07/.

[5] Accelerator Design and Construction for FFAG-KUCA ADSR, Y. Ishi, FFAG04 workshop, KEK, Tsukuba, http://hadron.kek.jp/FFAG/FFAG04_HP/index.html.

[6] 10 MW Non-scaling, non-linear FFAG SNS, G.H. Rees, FFAG 2007 Workshop, LPSC, Grenoble. http://lpsc.in2p3.fr/congres/FFAG07/.

[7] Development of FFAG accelerators and their applications for intense secondary particle production, Y. Mori, NIM A 562-2, 23 June 2006, 591-595.

[8] Study of Compact Medical FFAG Accelerators, Toshiyuki Misu, FFAG04 workshop, KEK, Tsukuba, http://hadron.kek.jp/FFAG/FFAG04_HP/index.html.

[9] The RACCAM Project, F. Méot et als., Proc. EPAC 2006 Conf.

[10] RACCAM, http://wwwlpsc.in2p3.fr/RACCAM/.

[11] (a) The ray-tracing code Zgoubi, F. Méot, NIM A 427 (1999) 353-356, and also
(b) Zgoubi users' guide, F. Méot and S. Valero, CEA DAPNIA SEA-97-13 and FERMILAB-TM-2010 (1997).

[12] Developments in the ray-tracing code Zgoubi for 6-D multiturn tracking in FFAG rings, F. Méot, F. Lemuet, NIM A 547 (2005) 638-651 ;
see also, Status of 6-D transmission simulations in FFAGs, F. Méot, FFAG05 Wrkshp, KURRI Institute, Kyoto, 5-9 Dec. 2005.

[13] FFAG Particle Accelerators, K. R. Symon et als., Phys. Rev. 103 (6), 1837 (1956).

[14] Deflecting magnets, H.A. Enge, in *Focusing of charged particles*, Vol. 2, A. Septier ed., Academic Press, New-York and London (1967).

[15] Optics and magnetic field map for a spiral FFAG, Florence Martinache, int. report IN2P3/LPSC, Grenoble (2006).

[16] Ray-tracing simulations in spiral sector FFAG magnets using Zgoubi code, J. Fourrier, int. report IN2P3/LPSC, Grenoble (2007).
See also, FFAG 2007 Workshophttp : //lpsc.in2p3.fr/congres/FFAG07/.

[17] Defect studies in the NuFact bow-tie muon storage ring, F. Méot, report IN2P3/LPSC LPSC 07-40 (2007).